Journal of Sol-Gel Science and Technology (2021) 99:109–121
https://doi.org/10.1007/s10971-021-05556-4

ORIGINAL PAPER: NANO-STRUCTURED MATERIALS (PARTICLES, FIBERS, COLLOIDS, COMPOSITES, ETC.)

Photocatalytic activity of Fe and Cu co-doped TiO_2 nanoparticles under visible light

Charitha Thambiliyagodage[1] · Shanitha Mirihana[1]

Received: 28 December 2020 / Accepted: 17 May 2021 / Published online: 31 May 2021

Abstract

The photocatalytic activity of single transition metal-doped TiO_2 nanoparticles is well established. This article reports the synthesis of Fe and Cu co-doped TiO_2 nanoparticles with varying Fe and Cu concentrations by the sol–gel method and their photocatalytic activity towards photodegradation of methylene blue under visible light. Nanoparticles were characterized by X-ray diffractometry (XRD), Raman spectroscopy, Transmission electron microscopy (TEM), Scanning electron microscopy (SEM), X-ray photoelectron spectroscopy (XPS), X-ray fluorescence spectroscopy (XRF), and Diffuse reflectance UV–Visible spectroscopy. XRD patterns revealed the existence of both anatase and rutile phases which was confirmed by Raman and TEM analysis. Both XRD and Raman analysis confirmed the successful doping of Fe and Cu without causing any significant lattice distortions. Nanoparticles were aggregated as shown in TEM and SEM images. XPS analysis revealed the presence of the only Ti^{4+} in pure TiO_2 while both Ti^{4+} and Ti^{3+} were present in doped TiO_2 in addition to Fe^{3+}, $Cu^{+,}$ and Cu^{2+}. XRF analysis showed the presence of only Ti, Fe, and Cu in the co-doped nanoparticles. According to the diffuse reflectance spectroscopic analysis, the visible light sensitivity of TiO_2 has increased upon doping with Fe and Cu. Single metal-doped nanoparticles were efficient than the co-doped nanoparticles for the degradation of methylene blue under visible light. Among the single doped nanoparticles, 0.05 Cu/TiO_2 showed the highest rate constant (0.0195 min^{-1}) while the maximum activity from the co-doped nanoparticles resulted in 0.05 Cu + 0.05 Fe/TiO_2 (0.0098 min^{-1}). The photocatalytic activity was decreased upon increasing the dopant (Fe/Cu) concentration due to the recombination of photogenerated electron-hole pairs, while due to the shielding effect, low photocatalytic activity resulted in co-doped nanoparticles with varying Fe and Cu loadings.

Graphical Abstract

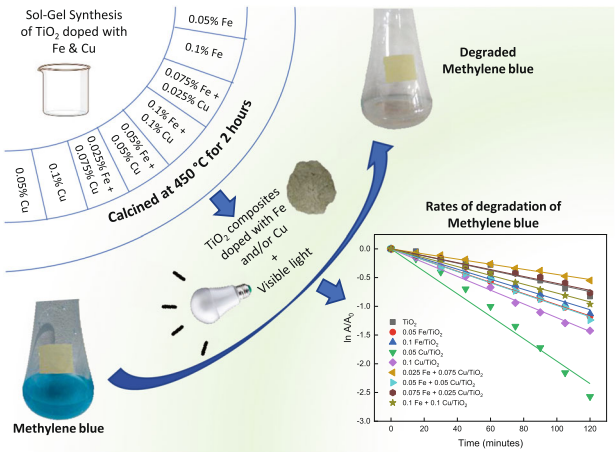

✉ Charitha Thambiliyagodage
charitha.t@sliit.lk

[1] School of Science and Education, Sri Lanka Institute of Information Technology, New Kandy Road, Malabe, Sri Lanka

Keywords Sol–gel synthesis · Photodegradation · Ti^{3+} · Fe^{3+} · Cu^{+} · Cu^{2+}

Highlights

- Cu and Fe co-doped TiO_2 nanoparticles with varying dopant concentrations were synthesized by the sol–gel method.
- Single doped TiO_2 nanoparticles are efficient in photodegrading methylene blue than co-doped TiO_2 nanoparticles under visible light.
- Photocatalytic activity of single doped TiO_2 nanoparticles is affected by electron-hole pair recombination and that of co-doped TiO_2 nanoparticles is influenced by both recombination and shielding effect.

1 Introduction

Dyes are abundantly released to normal water reservoirs from various industries including textile, rubber, carpet, food, plastics, and cosmetics, etc. [1–4]. They cause severe adverse effects such as increase chemical oxygen demand of the effluent and toxicity, reduce light penetration and hence limit photosynthesis. Further, the accumulation of dyes in water damage the aesthetic nature of the environment. Most of the dyes are stable for a long time being stable to light and oxidation and being resistant to aerobic degradation. Therefore, it is mandatory to remove these dyes from the effluents before they discharge to the water reservoirs. Hence, there is a need for a dye removal technique that could be used for larger scales and cost-effective [5]. Various methods are available to remove dyes from wastewater including membrane separation [6], adsorption [7], filtration [8], flotation [9], chemical oxidation [10], reverse osmosis [11] etc. Although these methods have been extensively studied they possess different disadvantages including high initial capital cost, the requirement of different chemicals, ineffective in removing all the pollutants, non-destruction of the pollutants, etc. [12].

Advanced oxidation processes (AOP) are highly active towards the degradation of organic and inorganic compounds that are resistant to conventional treatment methods. AOP produces reactive species, mainly hydroxyl radicals which help in degrading the target molecules to produce CO_2, H_2O, and mineral acids if the pollutants contain halogens [13]. AOP has gained interest in the treatment of wastewater due to its high efficiency, low toxicity, low cost, and tunable properties that can be modified such as doping, size reduction [14]. Semiconductors are being used as the photocatalysts to generate the reactive species and hence to catalyze the degradation process. Many semiconductors are photocatalytically active, such as titanium dioxide, tungsten oxide, molybdenum oxide, cerium oxide [14]. Among them, TiO_2 is considered the most promising candidate due to its high photocatalytic activity, chemical stability, low toxicity, and low cost [15]. However, TiO_2 possesses several disadvantages including inefficient exploitation of visible light, low adsorption capacity for hydrophobic contaminants, difficulty in post-treatment recovery, etc. [16]. TiO_2 exists in three main polymorphs as rutile (tetragonal), anatase (tetragonal), brookite (rhombohedral). Experimentally observed band gaps (E_g) of the polymorphs vary as E_g (rutile) $< E_g$ (anatase) $< E_g$ (brookite) where E_g of rutile is generally 3.0 eV. Therefore, it is evident that all the polymorphs of TiO_2 are active in the UV region being inefficient in visible light harvesting. Further, the rate of recombination of photogenerated species electron-hole pairs is also high in TiO_2. Hence, to improve visible light sensitivity many approaches have been implemented. Mainly doping TiO_2 with metals and/or non-metals has shown to improve the photocatalytic activity of TiO_2 by increasing the visible light sensitivity and impeding the electron-hole pair recombination. Many transition metals such as Fe [17–19], Cu [20, 21], Mo [22, 23], V [24, 25], Co [26, 27] non-metals including N [28, 29], S [30, 31], C [32], doped TiO_2 have shown promising photocatalytic activity in the visible region.

In the present study, the effect of doping TiO_2 with two transition metals, Fe and Cu which get doped via two mechanisms have been studied. Fe^{3+} is supposed to dope via substitution as the cationic radii of Fe^{3+} (0.745 Å) and Ti^{4+} (0.785 Å) are quite similar. But as Cu^{2+} (0.870 Å) ions are much larger than Ti^{4+} they may get incorporated into interstitial positions of the lattice. Further, Cu is in the same group of gold and silver in the periodic table and has similar properties due to its electronic configuration and the face centered cubic structure of the atom's location. Moreover, Cu can exist as copper oxides Cu_2O and CuO creating heterojunctions with TiO_2. Hence as Cu has different means of enhancing the photocatalytic activity of TiO_2, the effect of co-doping Fe and Cu on photocatalytic activity has been studied. Doped nanoparticles were synthesized by the sol–gel synthesis method and their photocatalytic activity was evaluated on the degradation of methylene blue under visible light exposure.

2 Materials and methods

2.1 Materials

Titanium isopropoxide (99%), $Fe(NO_3)_2$. $9H_2O$ (99%), $Cu(NO_3)_2.5H_2O$ (98%), ethanol, and nitric acid (70%), methylene

Table 1 Molar percentages of dopants (Fe and Cu) relative to TiO_2

Catalyst	%Fe	%Cu
TiO_2	0	0
0.05 Fe/TiO_2	0.05	0
0.1 Fe/TiO_2	0.1	0
0.05 Cu/TiO_2	0	0.05
0.1 Cu/TiO_2	0	0.1
0.025 Fe + 0.075 Cu/TiO_2	0.025	0.075
0.05 Fe + 0.05 Cu/TiO_2	0.05	0.05
0.075 Fe + 0.025 Cu/TiO_2	0.075	0.025
0.1 Fe + 0.1 Cu/TiO_2	0.1	0.1

blue were procured from Sisco Research Laboratories (Pvt) Ltd, India, and used as such.

2.2 Methods

2.2.1 Sol–gel synthesis of TiO_2 catalysts

Solution A containing deionized water acidified by nitric acid was added drop-wise to solution B containing ethanol and titanium isopropoxide in a volume ratio of (3:1) and stirred for 24 h. The resultant wet product was dried at 80 °C for about 24 h and calcined at 450 °C for 2 h.

2.2.2 Synthesis of iron and copper doped TiO_2 catalysts

Iron and copper were doped in different molar percentages relative to TiO_2 as shown in Table 1.

Appropriate amounts of Fe/Cu/Fe and Cu were dissolved in ethanol before TTIP was added to prepare solution B. All the other steps were exactly similar to the synthesis of undoped TiO_2.

2.2.3 Photocatalytic activity

The photocatalytic activity of the synthesized catalysts was evaluated towards the degradation of methylene blue using visible light generated by 50 W LED. The light intensity at the sample was maintained at 90,000–100,000. The photocatalytic activity experiments were carried out by taking 200 mg of photocatalyst and 100 ml of 3 mg/L MB solution. The photodegradation studies were done for 2 h excluding the first 30 min during which the samples were kept under dark conditions to reach the adsorption-desorption equilibrium. Samples were constantly shaken during the period of analysis. Samples of 3 ml were withdrawn from the solutions and the absorbance spectrum was collected by using a UV–visible spectrophotometer.

3 Characterization

X-ray diffraction (XRD) analysis was carried out using an Advance Bruker system using CuKα (λ = 0.154 nm) radiation and 2θ varying from 5°–80° at a scan speed of 2°/min. Raman analysis was performed by a Bruker Senterra Raman microscope spectrophotometer. The morphology of the samples was observed by a High-Resolution Transmission Electron Microscope operating at 200 kV (JEOL - JEM–2100) and energy dispersive spectra (EDS) were collected by the same instrument with TEAM EDX software. The sample (1 µl) was mounted on a holey carbon copper grid and allowed to dry at room temperature before TEM analysis. SEM images and EDS spectra were collected by Hitachi SU6600 Analytical Variable Pressure FE-SEM (Field Emission Scanning Electron Microscope) and Oxford Instruments EDX with AZtec software. Samples were mounted onto the sample stub using carbon tapes and the images were taken after gold sputter coating for 15 s. XPS spectra were acquired by Thermo Scientific™ ESCALAB Xi^+ X-ray Photoelectron Spectrometer. The chemical composition of the samples was analyzed by X-ray fluorescence (XRF) using a HORIBA Scientific XGT −5200 X-ray analytical microscope equipped with a Rh anode X-ray tube operated at a maximum voltage of 50 kV. Shimadzu 1800 UV/Visible spectrophotometer utilizing a precision Czerny-Turner optical system was used to analyze diffuse reflectance spectra of the prepared powder samples. The measurements were carried out through the range of 190–1100 nm with a bandwidth of 1.0 nm (wavelength accuracy +/−0.1 nm). The absorbance of MB samples was measured by a Shimadzu UV-1990 double beam UV–Visible spectrophotometer. Raman analysis was performed by a Bruker Senterra Raman microscope spectrophotometer.

4 Results and discussion

4.1 XRD analysis

XRD patterns were collected to determine the crystallographic orientation of the synthesized photocatalysts. XRD patterns of the catalysts are shown in Fig. 1a. The main diffraction peaks at 25.3° and 27.4° of the XRD patterns shown in Fig. 1a can be indexed to the (101) plane of anatase and (110) plane of rutile phase, respectively indicating that both anatase and rutile phases are present in the catalysts. Furthermore, no Fe or Cu-related oxides or other impurities can be observed. This signifies that the dopants are successfully doped into the lattice of TiO_2 or Fe and Cu ions are uniformly distributed on the surface of TiO_2 with quantities too low to be detected by XRD. Figure 1b shows the enlarged XRD peaks of the (101) plane of the anatase phase and the (110) of rutile. The XRD peak positions have shifted

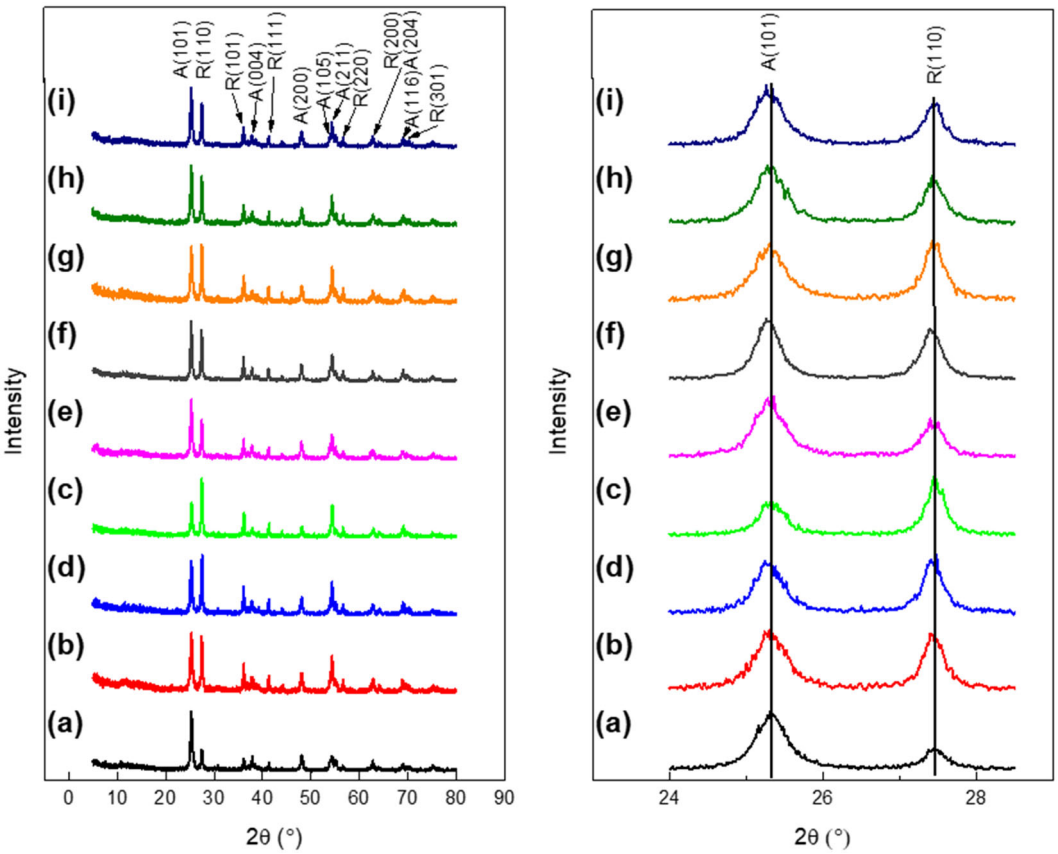

Fig. 1 **a** XRD patterns of (a) TiO_2, (b) 0.05 Fe/ TiO_2, (c) 0.05 Cu/ TiO_2, (d) 0.1 Fe/ TiO_2, (e) 0.1 Cu/ TiO_2, (f) 0.025 Fe + 0.075 Cu/ TiO_2, (g) 0.05 Fe + 0.05 Cu/ TiO_2, (h) 0.075 Fe + 0.025 Cu/ TiO_2, and (i) 0.1 Fe + 0.1 Cu/ TiO_2. **b** Enlarged region of 24°–28.5° showing the (101) plane of anatase phase and the (110) of rutile

towards a lower angle after doping with Fe^{3+} and Cu^{2+} slightly. The XRD peaks of crystal planes (101) and (200) in anatase were selected to determine the lattice parameters *a*, *b* and *c*, with Bragg's law employing tetragonal formula,

$$1/d^2 = h^2/a^2 + k^2/b^2 + l^2/c^2$$

Where d is the distance between adjacent lattice planes, *a*, *b*, and *c* are lattice constants and *h*, *k*, *l* are lattice vectors in Miller index notation. Calculated lattice parameters are tabulated in Table 1. Both *a* ($a = b$) and *c* lattice parameters of the doped nanomaterials are different from the pure TiO_2. Based on these observations, Fe^{3+} and Cu^{2+} have successfully doped into the lattice of TiO_2. These two modes of doping of metals into metal oxides as interstitial and substitution doping. The doping mode is determined by the electronegativity and the ionic radius of the doping ions. If the electronegativity and the ionic radius of doping ions match with those of the lattice ions, the dopant can substitute the lattice ions. Electronegativity of Ti^{4+}, Fe^{3+} and Cu^{2+} are 1.5, 1.8 and 1.9, respectively. Ionic radius of those are 0.745, 0.785 Å (high spin) and 0.870 Å, respectively [33]. Electronegativity values of Ti^{4+}, Fe^{3+}, and Cu^{2+} are compatible, however, when ionic radii are considered only the ionic radius of Fe^{3+} is quite similar to that of Ti^{4+}. Hence Fe^{3+} dopes to TiO_2 lattice substituting Ti^{4+}. However, the ionic radius of Cu^{2+} is higher than that of Ti^{4+}. Therefore, Cu^{2+} ions are most likely located in the interstitial positions in the lattice rather than directly in Ti^{4+} sites due to the relatively large size of the Cu^{2+} ions [33, 34]. Therefore, the doping mechanism of Fe^{3+} and Cu^{2+} could be summarized as substitution and interstitial doping, respectively. The d spacing between the atomic planes of each catalyst was calculated by considering (101) plane of anatase using the following equation,

$$\lambda = 2d\,sin\theta$$

where λ is the wavelength of the X-ray in nm (0.154 nm for Cu source). No significant influence on the d spacing value upon doping of TiO_2 was observed.

The crystallite sizes of the undoped and doped catalysts were calculated by using Scherrer's equation,

$$\tau = (0.9\lambda)/(\beta\,cos\theta),$$

where β is the full width at half maximum (FWHM) in radians. (101) plane of anatase plane was selected for the

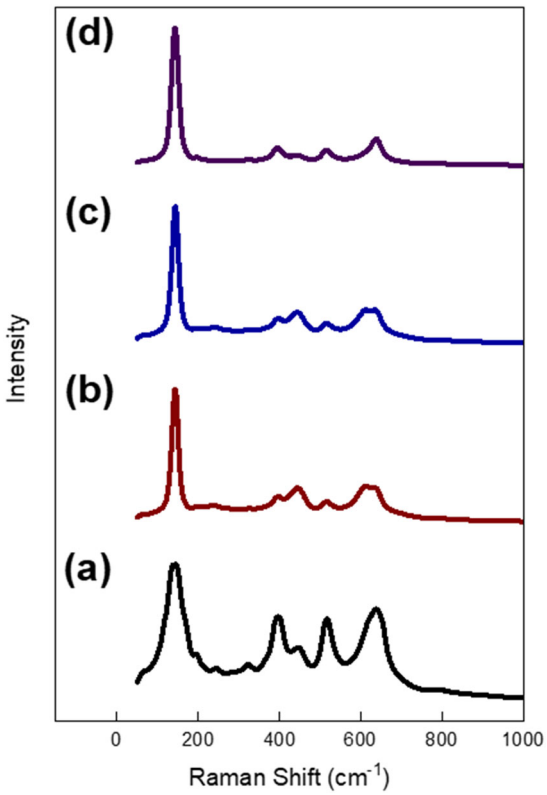

Fig. 2 Raman spectra of (**a**) TiO_2, (**b**) 0.1 Fe/TiO_2, (**c**) 0.1 Cu/TiO_2, and (**d**) 0.1 Fe + 0.1 Cu/TiO_2

calculation of crystallite size. As can be seen in the values tabulated in Table 1, no significant trend of the crystallite size was observed on doping TiO_2 by Fe^{3+} and Cu^{2+} with different doping concentrations.

4.2 Raman analysis

The Raman spectra were acquired to confirm the crystal structure of the catalysts suggested by XRD analysis (Fig. 2). Five characteristic Raman modes of anatase TiO_2 with symmetries 144.5 (E_g), 197 (E_g), 396.5 (B_{1g}), 516 (A_{1g}), 637.5 (E_g) cm^{-1} were observed in the Raman spectrum of undoped TiO_2 [35]. Additional peaks at 244, 444 (E_g) and 612 (A_{1g}) cm^{-1} correspond to a vibrational mode of rutile being consistent with the XRD pattern indicating the presence of both anatase and rutile phases [36]. Similar Raman modes were observed in the Raman spectra of 0.1 Fe/TiO_2, 0.1 Cu/TiO_2, and 0.1 Fe + 0.1 Cu/TiO_2, and additional peaks corresponding to the oxides of Fe and Cu were absent indicating the proper doping of Fe^{3+} and Cu^{2+} without creating significant lattice distortions. However, the peak intensity ratio of the main peak at 144.5 cm^{-1} to the others has shown a reduction when dopants are present compared to the undoped TiO_2. Further, peaks at 444 and 612 cm^{-1} correspond to the rutile phase is clearly visible especially in 0.1 Fe/TiO_2, 0.1 Cu/TiO_2 and its presence is comparatively less prominent in pure TiO_2 and 0.1 Fe + 0.1 Cu/TiO_2. Dopants, Fe^{3+}, and Cu^{2+} should be successfully doped in other catalysts of which the dopant concentrations are lower than 0.1% with no lattice distortions as suggested by the Raman spectroscopic data obtained with the analyzed catalysts.

4.3 TEM analysis

TEM analysis was performed to study morphology at the nanoscale and to confirm the crystallographic orientation of the prepared catalysts resulted from XRD patterns. TEM images of TiO_2 are shown in Fig. 3. Bright-field image (Fig. 3a) shows spherical and irregular-shaped nanoparticles and they are aggregated. This could be due to the rapid hydrolysis of titanium isopropoxide catalyzed by diluted nitric acid. Further, the absence of a surfactant during the synthesis may have contributed to particle aggregation. High-resolution TEM image (Fig. 3b) shows the arrangement of the atomic planes and the d spacing calculated from the generated histogram is 0.3598 nm. The obtained d spacing value matches with the d spacing value calculated for (101) plane (0.3515 nm) of the anatase phase. Interplanar spacing calculated from the HRTEM image is different from that calculated from the XRD data. This is because that TEM imaging is a localized effect where a particular location of the sample is selected for imaging at the nanoscale, while at acquiring XRD pattern, a comparatively large area is selected. The selected area diffraction pattern (Fig. 3c) shows a diffused ring pattern. Rings correspond to the (101) and (211) planes of anatase and the (101) plane of rutile could be observed. Phase identification performed by XRD, Raman spectroscopy, and TEM do well agree with each other. Electron map collected (Fig. 3d) show the elemental distribution of nanoparticles consisting of Ti, O, and C where C represents the carbon grid and the electron maps of Ti and O (Fig. 3e and f, respectively) show the individual elemental distribution on nanoparticles. EDS spectrum (Fig. 3g) also supports that the nanoparticles consist only of Ti and O and no other impurities are present.

4.4 SEM analysis

SEM images were collected to study the morphology of the synthesized catalysts at the macroscale. As can be seen in the SEM images are shown in Fig. 4 and basically, nanoparticles have been aggregated during the sol–gel synthesis being consistent with the TEM images as discussed. Incorporation of metal ions during the synthesis have not affected the morphology of the catalysts because the morphology shown by the SEM image of the undoped TiO_2 (Fig. 4a) are similar to the SEM images of the metal-doped

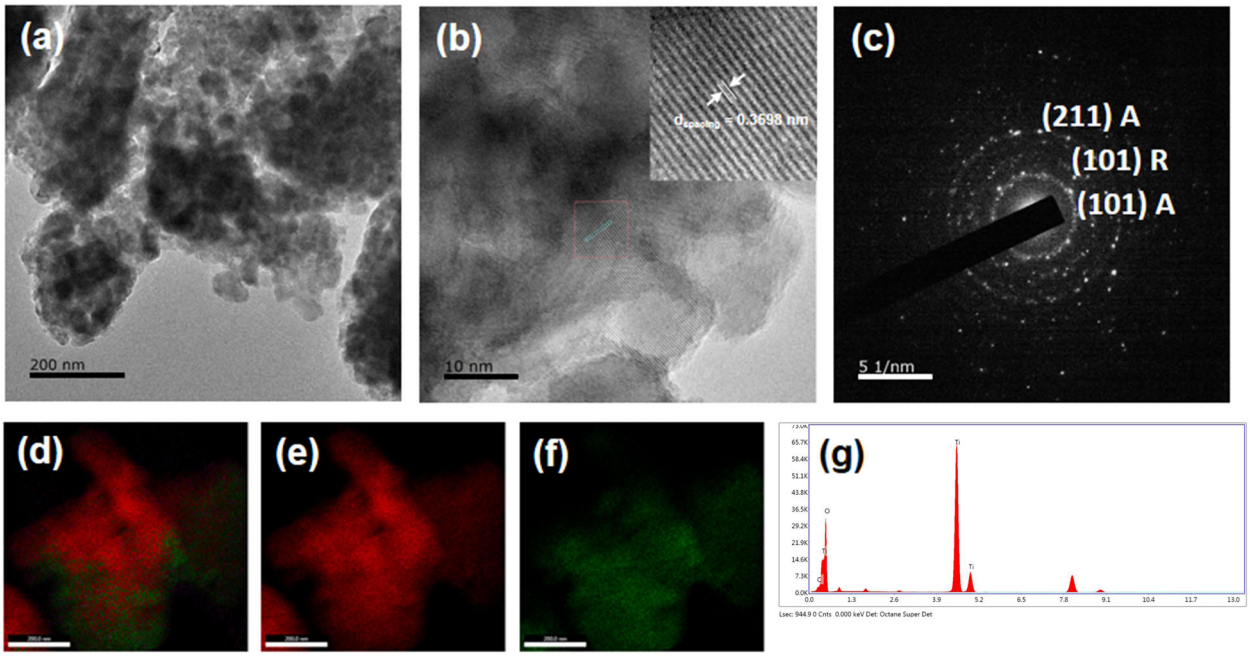

Fig. 3 **a** Bright filed image, **b** HRTEM image, **c** SADF, **d** Electron map of TiO_2, electron maps of (**e**) Ti, (**f**) O, and (**g**) EDX spectrum of TiO_2

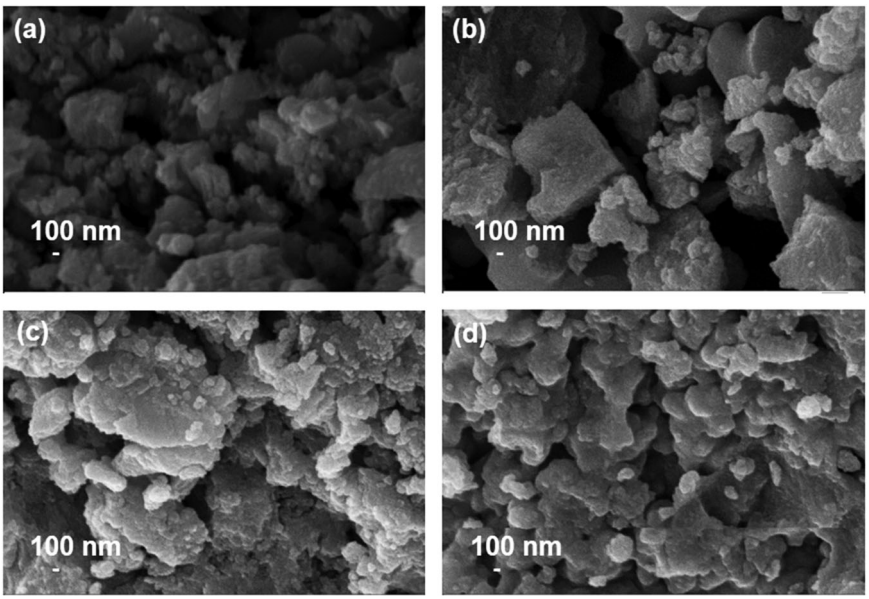

Fig. 4 SEM images of (**a**) TiO_2, (**b**) 0.05 Fe/TiO_2, (**c**) 0.05 Cu/TiO_2, and (**d**) 0.05 Fe + 0.05 Cu/TiO_2

nanoparticles, 0.05 Fe/TiO_2, 0.05 Cu/TiO_2, 0.05 Fe + 0.05 Cu/TiO_2 (Fig. 4b, c, d, respectively).

4.5 XPS analysis

To analyze the surface chemistry of the synthesized catalysts XPS analysis was performed (Fig. 5). The survey spectrum of pure TiO_2 (Fig. 5a) shows the presence of Ti, O, and C. The high resolution spectrum of Ti 2p is shown in Fig. 5a. In this spectrum doublet, Ti $2p_{3/2}$ (binding energy 459.8 eV) and Ti$2p_{1/2}$ (binding energy 465.58 eV) arise from the spin-orbital coupling. These peaks are consistent with the Ti^{4+} of TiO_2 lattice [37]. The high-resolution spectrum of O 1 s of the same sample was deconvoluted into two peaks centered at 531 and 532.85 eV (Fig. 5b). The peak at 531 eV shows the presence of OH group with oxygen at the bridging oxygen site and the peak at 532.85 eV could be attributed to the OH group as a terminal group with oxygen attached to the five-coordinated Ti^{4+} with an O-Ti^{4+} covalent bond [38]. The high resolution spectrum of C 1 s (Fig. 5d) is deconvoluted into four peaks.

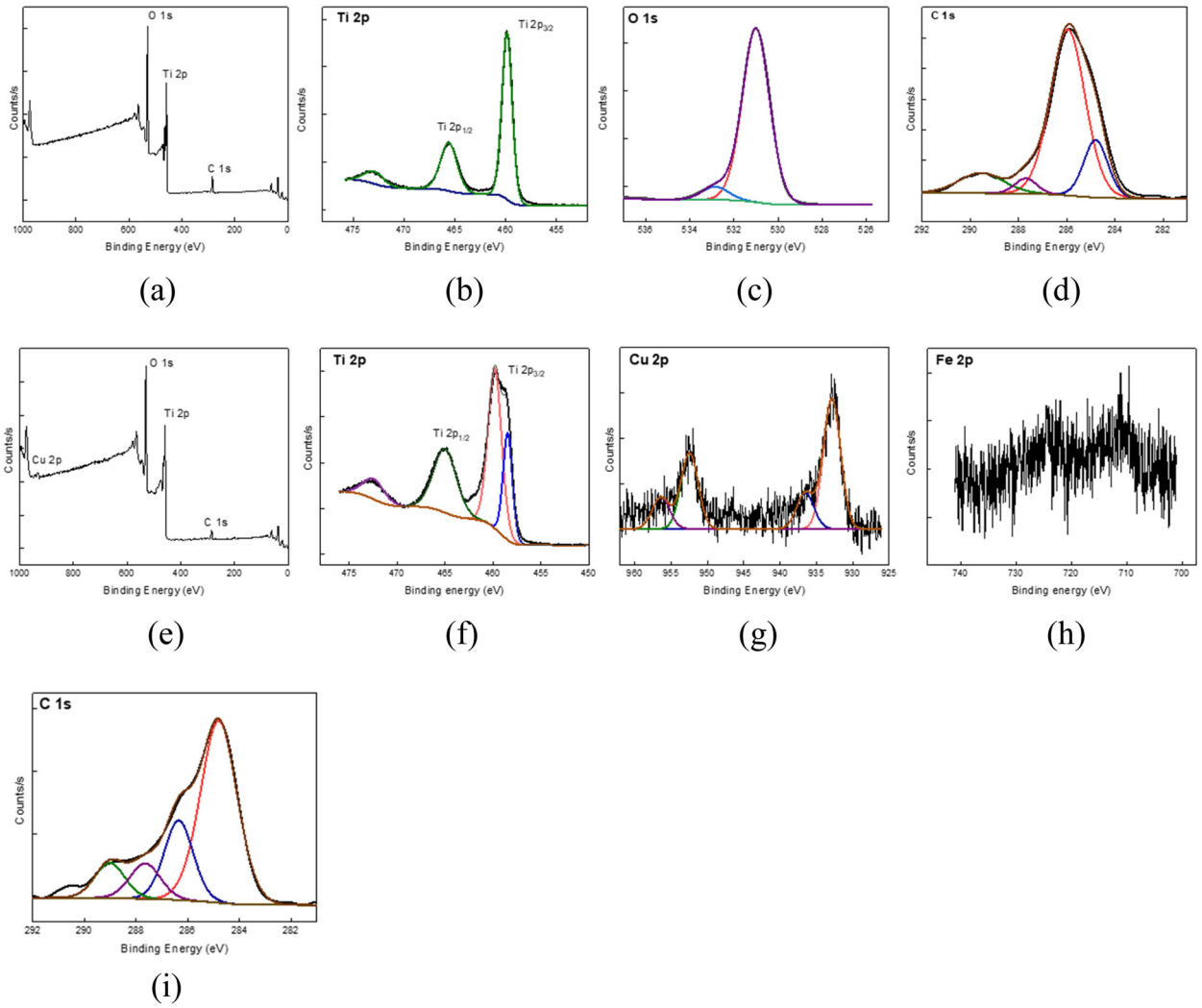

Fig. 5 **a** Survey spectrum, High resolution spectra of (**b**) Ti, (**c**) O, and (**d**) C of TiO_2. **e** Survey spectrum, High resolution spectra of (**f**) Ti, (**g**) Cu, (**h**) Fe, and (**i**) C of 0.1 Fe + 0.1 Cu/TiO_2

Peaks at 284.8, 286.35, 287.72, and 289.52 eV could be assigned to C–C, C–O, C=O, and O–C=O bonds [39]. The C/Ti ratio of pure TiO_2 is 0.13.

The survey spectrum of 0.1 Fe + 0.1 Cu/TiO_2 (Fig. 5e) shows the presence of Cu, Ti, O, and C. The high resolution spectrum of Ti of 0.1 Fe + 0.1 Cu/TiO_2 is shown in Fig. 5f. $2p_{3/2}$ peak was deconvoluted into two peaks centered at 459.8 eV and 458.45 eV and they correspond to the Ti^{4+} and Ti^{3+} oxidation states, respectively. The ratio between the Ti^{4+} to Ti^{3+} is approximately 2.17:1 calculated by the area under the curves. The high resolution spectrum of Cu (Fig. 5g) also shows the spin-orbital coupling, where, $2p_{3/2}$ and $2p_{1/2}$ peaks occurred at 932.87 and 952.46 eV, respectively, indicate the presence of Cu^{+}, while the peaks at 936.53 and 956.37 eV, show the presence of Cu^{2+} [40]. The ratio between the Cu^{+}/Cu^{2+} obtained from the area under the curves is 3.60. A similar observation was also reported by Akhaven et al. [41]. The high signal-to-noise ratio of the high-resolution spectrum of Fe (Fig. 5e) makes it difficult to identify the peaks. However, $2p_{3/2}$ and $2p_{1/2}$ have appeared at 711 and 724.57 eV, respectively revealing the presence of Fe^{3+} [42]. The high resolution spectrum of C 1 s (Fig. 5i) has been deconvoluted to four peaks. Peaks at 284.8, 286.35, 287.65, and 289.02 eV could be attributed to C–C, C–O, C=O, and O–C=O bonds [39]. Further, the Ti-C bond expected to appear at 283.7 eV [39, 43, 44] was not observed revealing that impurity C has not been doped to TiO_2 during the synthesis. It has been reported that carbon can form a Ti-C bond when treated the samples at 400 °C by Akhavan et al. [39, 43, 44]. The Cu/Ti and C/Ti ratios of the synthesized 0.1 Fe + 0.1 Cu/TiO_2 nanomaterial are 0.09 and 0.056, respectively.

4.6 X-ray fluorescence spectroscopic analysis

XRF analysis was performed on 0.1Cu + 0.1Fe/TiO_2 to identify the elemental distribution. Data tabulated in Table 2

Table 2 XRF analysis of 0.1Cu + 0.1Fe/TiO_2

Element	Spot 1 Mass %	Spot 2 Mass %	Spot 3 Mass %	Spot 4 Mass %	Spot 5 Mass %	Spot 6 Mass %
22 Ti	99.57	99.71	99.45	99.68	99.60	99.69
26 Fe	0.15	0.16	0.17	0.15	0.16	0.16
29 Cu	0.17	0.13	0.17	0.17	0.14	0.15

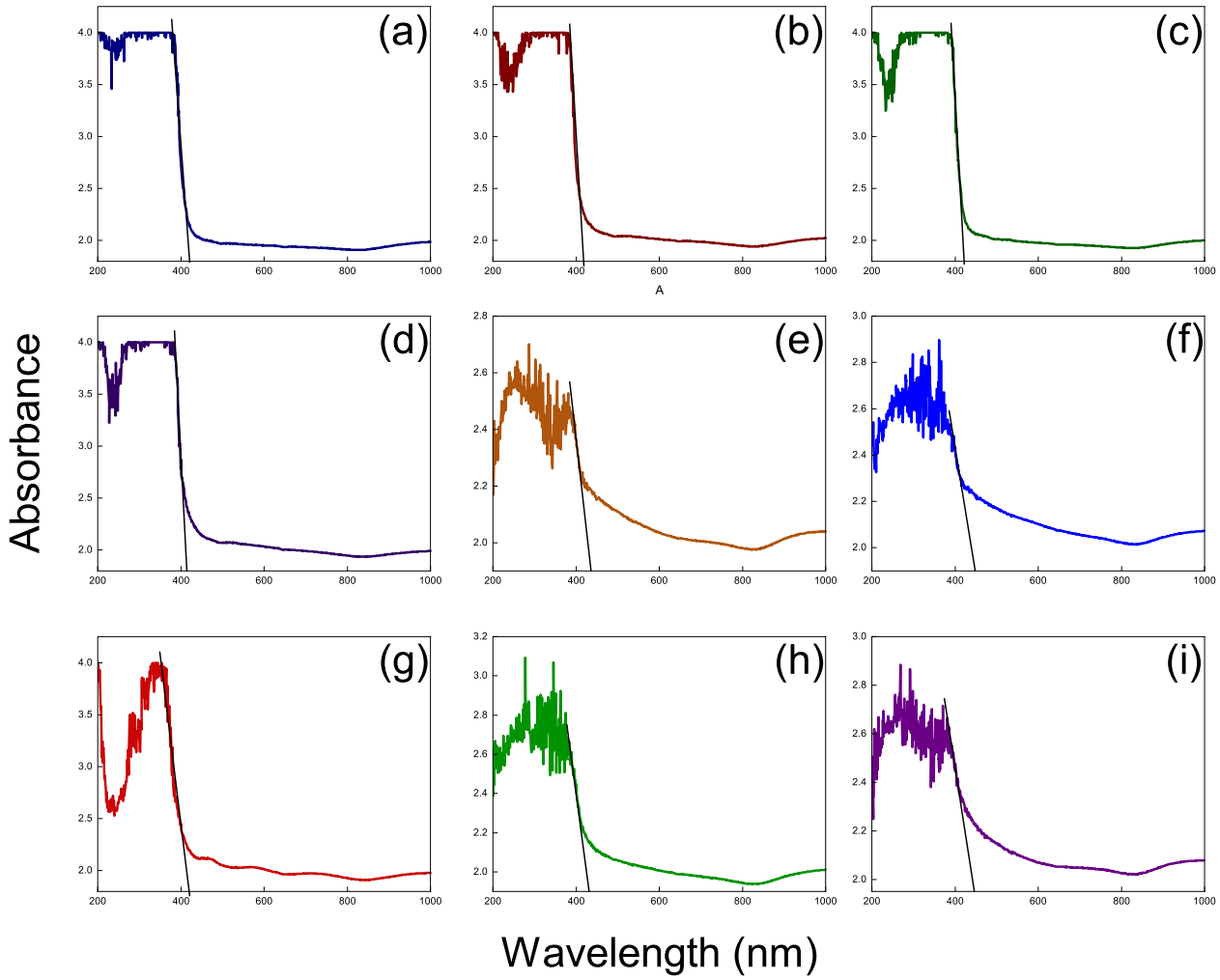

Fig. 6 Diffuse reflectance UV–Visible spectra of (**a**) TiO_2, (**b**) 0.05 Fe/ TiO_2, (**c**) 0.05 Cu/ TiO_2, (**d**) 0.1 Fe/ TiO_2, (**e**) 0.1 Cu/ TiO_2, (**f**) 0.025 Fe + 0.075 Cu/ TiO_2, (**g**) 0.05 Fe + 0.05 Cu/ TiO_2, (**h**) 0.075 Fe + 0.025 Cu/ TiO_2, and (**i**) 0.1 Fe + 0.1 Cu/ TiO_2

were collected from six different spots of the sample. The nanomaterials consist of Ti, Fe, and Cu only. The Fe: Cu ratio at all the analyzed spots is 1:1 showing the homogeneous distribution of the metal ions on the TiO_2 matrix.

4.7 Diffuse reflectance UV–Visible spectroscopic analysis

The electronic band structures of the prepared samples were analyzed by UV–Visible absorption spectroscopy (Fig. 6). Compared with the undoped TiO_2, doped TiO_2 show a higher light harvest performance reflected by the enhancement of light absorbance covering the visible range. To determine the band gap energies of the synthesized materials cutoff wavelengths were determined by drawing a tangent to the absorption curves. The band gap energy is calculated by the following equation,

$$E_{bg} = 1240/\lambda$$

Calculated band gap values are tabulated in Table 3. The band gap of pure TiO_2 (2.98 eV) is lesser than the reported

Table 3 d spacing, crystallite size, and lattice parameters calculated by the XRD patterns and the band gap energy calculated by diffuse reflectance spectroscopy

Compound	d spacing (nm)	Crystallite size (nm)	Lattice parameters (nm)			Bandgap (eV)
			a	b	c	
TiO_2	0.3515	18.0	0.3784	0.3784	0.9492	2.98
0.05 Fe/TiO_2	0.3495	15.9	0.3774	0.3774	0.9262	2.98
0.05 Cu/TiO_2	0.3507	19.3	0.3776	0.3776	0.9460	2.95
0.1 Fe/TiO_2	0.3506	20.3	0.3780	0.378	0.9379	2.98
0.1 Cu/TiO_2	0.3522	17.9	0.3786	0.3786	0.9599	2.85
0.025 Fe + 0.075 Cu/TiO_2	0.3522	23.2	0.3790	0.379	0.9535	2.75
0.05 Fe + 0.05 Cu/TiO_2	0.3524	17.6	0.3780	0.378	0.9741	2.96
0.075 Fe + 0.025 Cu/TiO_2	0.3517	18.0	0.3780	0.378	0.9596	2.88
0.1 Fe + 0.1 Cu/TiO_2	0.3524	18.4	0.3784	0.3784	0.9673	2.78

band gap energy for anatase (3.2 eV). As revealed by the XRD patterns, both anatase and rutile phases are present in pure TiO_2. Both $Ti^{4+}$and Ti^{3+} were identified in the high resolution XPS spectrum of Ti 2p of 0.1 Fe + 0.1 Cu/TiO_2. The decrease of the band gap can be due to the localized gap states induced by Ti^{3+} and to the oxygen vacancies [45–47]. Missing an oxygen atom from the surface or bulk of TiO_2 results in one or two electrons localized in an oxygen vacancy state. These electrons localized on the oxygen vacancy state form a donor level below the conduction band of TiO_2 [46]. In general transition metals like Fe doped TiO_2 show, relatively a lower band gap compared to the undoped TiO_2 due to the formation of a new energy level below the conduction band of TiO_2 due to the doping of Fe^{3+} and formation of Ti^{3+}. Moreover, transition metals like Cu and rare-earth metals like La, lead to the lattice deformation and the formation of oxygen vacancies, resulting in impurity states in the TiO_2 band gap, and hence narrow the band gap [48]. However, calculated band gap energies do not show a clear significant reduction in band gap upon doping increasing dopant (Fe and Cu) concentrations. It is reported that the band gap of semiconductors is affected by many factors including particle size, shape, surface area, etc. The band gap energy increases with decreasing particle size because of the confinement of electrons and holes. Volume to surface area ratio varies with the size and the shape of the materials that alter the number of surface atoms at the nanoscale and cohesive energy. Therefore the band gap energy changes at the nanoscale. When the particle size reaches the nanoscale, the number of overlapping orbitals or energy levels decreases, and the thickness of the band reduces. Then the energy gap between the valence band and the conduction band increases [49]. A clear relationship between the crystallite size calculated by XRD patterns and the band gap energies was not observed. According to the SEM images collected it could be seen that the particle size varies from one sample to the other. Hence, there cannot be a clear trend in the surface area as well. Therefore, as many factors collectively contribute to the band gap energy, resulted in variation cannot be exactly explained.

4.8 Photocatalytic activity

The photocatalytic activity of the prepared photocatalysts was evaluated on the degradation of MB under visible light. MB was selected as the model pollutant as it is extensively used in the industry. The degradation kinetics was computed by the change in MB concentration measured by UV–Visible spectrophotometer as a function of irradiation time (Fig. 7). The rate constants tabulated in Table 4 reveal that the photodegradation efficiency of the 0.05 Cu/TiO_2 (0.0195 min^{-1}) is higher than all the nanomaterials followed by 0.1 Cu/TiO_2 (0.0120 min^{-1}). As revealed by the XPS analysis, catalysts contain both Cu^+ and Cu^{2+}. Cu^+ is quite unstable during both the atmospheric and photocatalytic reaction conditions. Therefore, during the photocatalysis existing Cu^+ would probably oxidize to Cu^{2+}. Rate constant for the degradation of TiO_2 (0.0062 min^{-1}) is greater than that of 0.025 Fe + 0.075 Cu/TiO_2 (0.0044 min^{-1}) and similar to that of 0.075 Fe + 0.025 Cu/TiO_2 (0.0060 min^{-1}). The photodegradation efficiency of other photocatalysts was greater than that of TiO_2 as shown in Table 4. Therefore it is evident that the visible light sensitivity of TiO_2 has been enhanced by doping with Fe and Cu. Cu/TiO_2 has shown higher photocatalytic activity than Fe/TiO_2. Cu contributes to photocatalytic activity in several ways. Cu^{2+} dope to the interstitial positions of TiO_2 due to the difference of the valence state and the cationic radii [50, 51]. Cu can exist in a wide range of accessible oxidation states as Cu^0, $Cu^{I,}$ and Cu^{II}, and hence the active species in TiO_2 are Cu, Cu_2O, and CuO [34]. Metallic Cu exists in the same group of gold and silver of the periodic table has similar properties due to the electronic configuration and the face centered cubic (FCC) structure. Metallic Cu nanoparticles can activate TiO_2

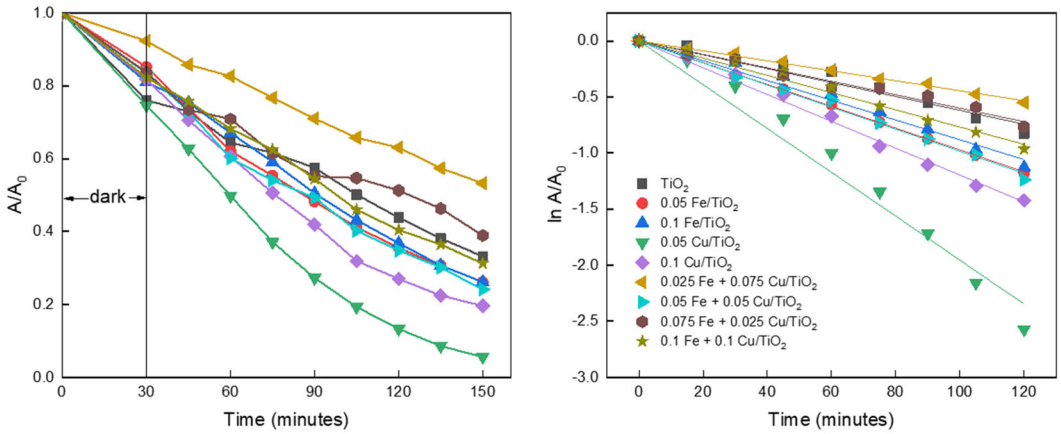

(a) (b)

Fig. 7 Photocatalytic activity of the synthesized photocatalysts. **a** Change in absorbance as a function of irradiation time. **b** Plot of ln A/A_0 as a function of irradiation time for the degradation of MB under visible light

Table 4 Rate constants of the prepared photocatalysts

Photocatalyst	Rate Constant (min^{-1})
TiO_2	0.0062
0.05 Fe/TiO_2	0.0097
0.05 Cu/TiO_2	0.0195
0.1 Fe/TiO_2	0.0088
0.1 Cu/TiO_2	0.0120
0.025 Fe + 0.075 Cu/TiO_2	0.0044
0.05 Fe + 0.05 Cu/TiO_2	0.0098
0.075 Fe + 0.025 Cu/TiO_2	0.0060
0.1 Fe + 0.1 Cu/TiO_2	0.0077

towards visible light due to the localized surface plasmon resonance (LSPR) effect. LSPR is excited when light interacts with the free electrons of the metallic nanostructure, which results in collective excitations that lead to significant improvement of the local electromagnetic fields surrounding the nanoparticles [52]. Once the visible light is absorbed by the Cu nanoparticle modified TiO_2, electrons are transferred to the conduction band of TiO_2, which creates an electron-deficient metal and rich TiO_2, where direct photocatalytic oxidation occurs on the metal surface. However, metallic Cu does not exist under normal atmospheric conditions because it gets oxidized in the presence of oxygen. The presence of metallic Cu was not evident even from the XPS analysis and hence it is clear that the LSPR effect has not contributed to the photocatalytic activity tested in the study. Copper oxides can form heterojunction systems with TiO_2. There are several advantages associated with heterojunctions including improvement of the charge carriers' separation, increase in the lifetime of the charge carrier, and enhancement of the interfacial charge transfer efficiency [53, 54]. Cu_2O and CuO are *p*-type semiconductors with band gap energies of 2.1 and 1.7 eV, respectively [34]. The most probable type of heterostructure for the Cu_xO/TiO_2 system would be probably type II, where photoexcited electrons are transferred from CB of Cu_xO to the CB of TiO_2 and photogenerated holes transferred simultaneously from the VB of TiO_2 to VB of Cu_xO. As a result, photogenerated electrons and holes are separated reducing the recombination and increasing the lifetimes of the charge carriers [55]. The presence of Cu^+ at the surface of the catalyst is confirmed by the XPS analysis. Therefore, both Cu_2O and CuO could be present in the prepared catalysts. As revealed by the XPS analysis Fe and Cu co-doped TiO_2, Ti^{3+} was present in addition to Ti^{4+}. The Ti^{3+} defects can form a shallow donor level just below the conduction band which enhances the visible light sensitivity [46]. Under visible light irradiation, induced electrons on an isolated Ti^{3+} band could be transferred to the surface of CuO nanoclusters efficiently, in addition to the direct charge transfer from the VB of TiO_2 improving the photocatalytic activity [56]. Further, photogenerated electrons from Cu_2O would be captured by Ti^{4+} ions in TiO_2 and get reduced to Ti^{3+}, increasing the Ti^{3+} concentration triggering the effect from Ti^{3+}. Whereas, left holes at the VB of Cu_2O hamper the charge recombination resulting in an improved photocatalytic activity [57]. Though an enhanced photocatalytic activity was observed with low Cu loading (0.05%), photocatalytic activity decreased with increasing the Cu loading (0.1%). This could be due to the shielding effect caused by the dispersed CuO nanoparticles covering the surface of TiO_2 reducing the photon adsorption. Moreover, a higher concentration of CuO could promote the photogenerated electron-hole pair recombination resulting in a decrease in available holes for redox reactions [58]. Fe is considered as a successful dopant because they dope via

substitution due to the quite similar cationic radii (Fe–0.745 Å, Ti–0.785 Å) and Fe^{3+} has a stable half-filled d^5 configuration. Rate constant of 0.05 Fe/ TiO_2 (0.0097 min^{-1}) is greater than that of 0.1 Fe/ TiO_2 (0.088 S^{-1}). With higher Fe loading comparatively low photocatalytic activity was observed due to the recombination of photogenerated electron and hole pairs. The main hypothesis of this study is to determine the effect of co-doping of Fe and Cu on photocatalytic activity. Fe and Cu have been doped in different proportions to study in detail the effect of co-doping on photocatalytic activity. The obtained rate constants for co-doped TiO_2 are lesser than single metal-doped TiO_2. Among the co-doped TiO_2 catalysts, TiO_2 doped with equal proportions of Fe and Cu showed comparatively higher photocatalytic activity for the degradation of MB (0.05 Fe + 0.05 Cu/ TiO_2 - 0.0098 min^{-1} and 0.1 Fe + 0.1 Cu/ TiO_2 is 0.0077 min^{-1}) and of these two higher Fe and Cu loading showed low activity due to the recombination of photo-generated electron-hole pairs. Catalysts prepared with unequal Fe and Cu proportions showed lower photocatalytic activity. 0.075 Fe + 0.025 Cu/ TiO_2 showed a similar activity to the pure TiO_2 (0.0060 min^{-1}) while the photocatalytic activity of 0.025 Fe + 0.075 Cu/ TiO_2 (0.0044 min^{-1}) was lower than pure TiO_2. This could be due to the masking effect of one metal by the other as well as the shielding effect of TiO_2 by both metals. Moreover, the lowest photocatalytic activity has resulted with the photocatalyst with higher Cu loading because though Cu_xO is present as the TiO_2 is shielded proper charge migration and separation at the heterojunction would have not taken place.

5 Conclusion

Fe and Cu co-doped TiO_2 nanoparticles with varying Fe and Cu were synthesized by the sol–gel method. The crystal structure of TiO_2 has not deteriorated by doping of Fe and Cu. The doping of Fe is confirmed to be mainly +3, which provides extra electronic states in the band gap of TiO_2. Doped Cu form heterojunction of Cu_xO/TiO_2 that facilitate the charge separation. The absorption edge of TiO_2 is shifted to the visible region by doping with Fe and Cu. Single doping of Fe and Cu has significantly improved the photocatalytic activity while co-doping has resulted in comparatively low photocatalytic activity on photodegradation of methylene blue under visible light irradiation. 0.05 Cu/ TiO_2 showed the highest photocatalytic activity among the single doped systems while the highest photocatalytic activity of the co-doped systems was obtained from 0.05 Cu + 0.05 Fe/ TiO_2. Low photocatalytic activity with higher metal loading at single doping was resulted due to the electron-hole pair recombination while the low activity of co-doping systems has caused by the shielding effect of each dopant and TiO_2 by the doped metals.

Acknowledgements The authors acknowledge the Sri Lanka Institute of Information Technology for providing the funds. The authors are much grateful to the Sri Lanka Institute of nanotechnology for facilitating the project with the required instruments.

Funding This project was funded by a research grant awarded by Sri Lanka Institute of Information Technology.

Compliance with ethical standards

Conflict of interest The authors declare no competing interests.

References

1. Arami M, Limaee NY, Mahmoodi NM, Tabrizi NS (2005) Removal of dyes from colored textile wastewater by orange peel adsorbent: Equilibrium and kinetic studies. J Colloid Interface Sci 288:371–376. https://doi.org/10.1016/j.jcis.2005.03.020
2. Robinson T, Chandran B, Nigam P (2002) Removal of dyes from a synthetic textile dye effluent by biosorption on apple pomace and wheat straw. Water Res 36:2824–2830. https://doi.org/10.1016/S0043-1354(01)00521-8
3. Ramakrishna KR, Viraraghavan T (1997) Dye removal using low cost adsorbents. Water Sci Technol 189–196. https://doi.org/10.1016/S0273-1223(97)00387-9
4. Nigam P, Armour G, Banat IM et al. (2000) Physical removal of textile dyes from effluents and solid-state fermentation of dye-adsorbed agricultural residues. Bioresour Technol 72:219–226. https://doi.org/10.1016/S0960-8524(99)00123-6
5. Mohan D, Singh KP, Singh G, Kumar K (2002) Removal of dyes from wastewater using flyash, a low-cost adsorbent. Ind Eng Chem Res 41:3688–3695. https://doi.org/10.1021/ie010667+
6. Jirankova H, Mrazek J, Dolecek P, Cakl J (2010) Organic dye removal by combined adsorption-membrane separation process. Desalin Water Treat 20:96–101. https://doi.org/10.5004/dwt.2010.1170
7. Robinson T, Chandran B, Nigam P (2002) Removal of dyes from a synthetic textile dye effluent by biosorption on apple pomace and wheat straw. Water Res 36:2824–2830. https://doi.org/10.1016/S0043-1354(01)00521-8
8. Lafi R, Gzara L, Lajimi RH, Hafiane A (2018) Treatment of textile wastewater by a hybrid ultrafiltration/electrodialysis process. Chem Eng Process - Process Intensif 132:105–113. https://doi.org/10.1016/j.cep.2018.08.010
9. Mohammed AA, Ebrahim SE, Alwared AI (2013) Flotation and sorptive-flotation methods for removal of lead ions from wastewater using SDS as surfactant and barley husk as biosorbent. J Chem https://doi.org/10.1155/2013/413948
10. Brisset J-L, Benstaali B, Moussa D et al. (2011) Acidity control of plasma-chemical oxidation: applications to dye removal, urban waste abatement and microbial inactivation. Plasma Sources Sci Technol 20:34021. https://doi.org/10.1088/0963-0252/20/3/034021
11. Abid MF, Zablouk MA, Abid-Alameer AM (2012) Experimental study of dye removal from industrial wastewater by membrane technologies of reverse osmosis and nanofiltration. Iran J Environ Health Sci Eng 9:17. https://doi.org/10.1186/1735-2746-9-17
12. Crini G, Lichtfouse E (2019) Advantages and disadvantages of techniques used for wastewater treatment. Environ Chem Lett 17:145–155. https://doi.org/10.1007/s10311-018-0785-9

13. Joseph CG, Li Puma G, Bono A, Krishnaiah D (2009) Sonophotocatalysis in advanced oxidation process: a short review. Ultrason Sonochem 16:583–589. https://doi.org/10.1016/j.ultsonch.2009.02.002
14. Chan SHS, Yeong Wu T, Juan JC, Teh CY (2011) Recent developments of metal oxide semiconductors as photocatalysts in advanced oxidation processes (AOPs) for treatment of dye wastewater. J Chem Technol Biotechnol 86:1130–1158. https://doi.org/10.1002/jctb.2636
15. Saien J, Asgari M, Soleymani AR, Taghavinia N (2009) Photocatalytic decomposition of direct red 16 and kinetics analysis in a conic body packed bed reactor with nanostructure titania coated Raschig rings. Chem Eng J 151:295–301. https://doi.org/10.1016/j.cej.2009.03.011
16. Dong H, Zeng G, Tang L et al. (2015) An overview on limitations of TiO_2-based particles for photocatalytic degradation of organic pollutants and the corresponding countermeasures. Water Res 79:128–146. https://doi.org/10.1016/j.watres.2015.04.038
17. Ismael M (2020) Enhanced photocatalytic hydrogen production and degradation of organic pollutants from Fe (III) doped TiO_2 nanoparticles. J Environ Chem Eng 8:103676. https://doi.org/10.1016/j.jece.2020.103676
18. Cheng G, Liu X, Song X et al. (2020) Visible-light-driven deep oxidation of NO over Fe doped TiO_2 catalyst: synergic effect of Fe and oxygen vacancies. Appl Catal B Environ 277:119196. https://doi.org/10.1016/j.apcatb.2020.119196
19. Akhavan O (2010) Thickness dependent activity of nanostructured TiO_2/α-Fe_2O_3 photocatalyst thin films. Appl Surf Sci 257:1724–1728. https://doi.org/10.1016/j.apsusc.2010.09.005
20. Yang WT, Lin CJ, Montini T et al. (2021) High-performance and long-term stability of mesoporous Cu-doped TiO_2 microsphere for catalytic CO oxidation. J Hazard Mater 403:123630. https://doi.org/10.1016/j.jhazmat.2020.123630
21. Ikram M, Umar E, Raza A et al. (2020) Dye degradation performance, bactericidal behavior and molecular docking analysis of Cu-doped TiO_2 nanoparticles. RSC Adv 10:24215–24233. https://doi.org/10.1039/d0ra04851h
22. Huang J, Guo X, Wang B et al. (2015) Synthesis and photocatalytic activity of Mo-doped TiO_2 nanoparticles. J Spectrosc 2015:681850. https://doi.org/10.1155/2015/681850
23. Kumaravel V, Rhatigan S, Mathew S et al. (2020) Mo doped TiO_2: impact on oxygen vacancies, anatase phase stability and photocatalytic activity. J Phys Mater 3:25008. https://doi.org/10.1088/2515-7639/ab749c
24. Klosek S, Raftery D (2002) Visible light driven V-doped TiO_2 photocatalyst and its photooxidation of ethanol. J Phys Chem B 105:2815–2819. https://doi.org/10.1021/jp004295e
25. Avansi W, Arenal R, De Mendonça VR et al. (2014) Vanadium-doped TiO_2 anatase nanostructures: the role of v in solid solution formation and its effect on the optical properties. CrystEngComm 16:5021–5027. https://doi.org/10.1039/c3ce42356e
26. Santara B, Pal B, Giri PK (2011) Signature of strong ferromagnetism and optical properties of Co doped TiO_2 nanoparticles. J Appl Phys 110:114322. https://doi.org/10.1063/1.3665883
27. Barakat MA, Schaeffer H, Hayes G, Ismat-Shah S (2005) Photocatalytic degradation of 2-chlorophenol by Co-doped TiO_2 nanoparticles. Appl Catal B Environ 57:23–30. https://doi.org/10.1016/j.apcatb.2004.10.001
28. Fiorenza R, Di Mauro A, Cantarella M et al. (2020) Molecularly imprinted N-doped TiO_2 photocatalysts for the selective degradation of o-phenylphenol fungicide from water. Mater Sci Semicond Process 112:105019. https://doi.org/10.1016/j.mssp.2020.105019
29. Kovalevskiy N, Selishchev D, Svintsitskiy D et al. (2020) Synergistic effect of polychromatic radiation on visible light activity of N-doped TiO_2 photocatalyst. Catal Commun 134:105841. https://doi.org/10.1016/j.catcom.2019.105841
30. Pillai VV, Lonkar SP, Alhassan SM (2020) Template-free, solid-state synthesis of hierarchically macroporous S-doped TiO_2 nanophotocatalysts for efficient water remediation. ACS Omega 5:7969–7978. https://doi.org/10.1021/acsomega.9b04409
31. Chen X, Sun H, Zelekew OA et al. (2020) Biological renewable hemicellulose-template for synthesis of visible light responsive sulfur-doped TiO_2 for photocatalytic oxidation of toxic organic and As(III) pollutants. Appl Surf Sci 525:146531. https://doi.org/10.1016/j.apsusc.2020.146531
32. Zhao D, Zhang X, Sui L et al. (2020) C-doped TiO_2 nanoparticles to detect alcohols with different carbon chains and their sensing mechanism analysis. Sens Actuators B Chem 312:127942. https://doi.org/10.1016/j.snb.2020.127942
33. Choi J, Park H, Hoffmann MR (2010) Effects of single metal-ion doping on the visible-light photoreactivity of TiO_2. J Phys Chem C 114:783–792. https://doi.org/10.1021/jp908088x
34. Janczarek M, Kowalska E (2017) On the origin of enhanced photocatalytic activity of copper-modified titania in the oxidative reaction systems. Catalysts 7:317. https://doi.org/10.3390/catal7110317
35. Hardcastle FD (2011) Raman spectroscopy of titania (TiO_2) nanotubular water-splitting catalysts. J Ark Acad Sci 65:9, https://scholarworks.uark.edu/jaas/vol65/iss1/9
36. Balachandran U, Eror NG (1982) Raman spectra of titanium dioxide. J Solid State Chem 42:276–282. https://doi.org/10.1016/0022-4596(82)90006-8
37. Sanjinés R, Tang H, Berger H et al. (1994) Electronic structure of anatase TiO_2 oxide. J Appl Phys 75:2945–2951. https://doi.org/10.1063/1.356190
38. Krishnan P, Liu M, Itty PA et al. (2017) Characterization of photocatalytic TiO_2 powder under varied environments using near ambient pressure X-ray photoelectron spectroscopy. Sci Rep. 7:1–11. https://doi.org/10.1038/srep43298
39. Akhavan O, Abdolahad M, Abdi Y, Mohajerzadeh S (2009) Synthesis of titania/carbon nanotube heterojunction arrays for photoinactivation of E. coli in visible light irradiation. Carbon N. Y 47:3280–3287. https://doi.org/10.1016/j.carbon.2009.07.046
40. Biesinger MC (2017) Advanced analysis of copper X-ray photoelectron spectra. Surf Interface Anal 49:1325–1334. https://doi.org/10.1002/sia.6239
41. Akhavan O, Tohidi H, Moshfegh AZ (2009) Synthesis and electrochromic study of sol-gel cuprous oxide nanoparticles accumulated on silica thin film. Thin Solid Films 517:6700–6706. https://doi.org/10.1016/j.tsf.2009.05.016
42. Yamashita T, Hayes P (2008) Analysis of XPS spectra of Fe2+ and Fe3+ ions in oxide materials. Appl Surf Sci 254:2441–2449. https://doi.org/10.1016/j.apsusc.2007.09.063
43. Akhavan O, Ghaderi E (2009) Photocatalytic reduction of graphene oxide nanosheets on TiO_2 thin film for photoinactivation of bacteria in solar light irradiation. J Phys Chem C 113:20214–20220. https://doi.org/10.1021/jp906325q
44. Akhavan O, Ghaderi E (2013) Flash photo stimulation of human neural stem cells on graphene/TiO_2 heterojunction for differentiation into neurons. Nanoscale 5:10316–10326. https://doi.org/10.1039/c3nr02161k
45. Liu X, Gao S, Xu H et al. (2013) Green synthetic approach for Ti^{3+} self-doped TiO_{2-x} nanoparticles with efficient visible light photocatalytic activity. Nanoscale 5:1870–1875. https://doi.org/10.1039/c2nr33563h
46. Pan X, Yang MQ, Fu X et al. (2013) Defective TiO_2 with oxygen vacancies: Synthesis, properties and photocatalytic applications. Nanoscale 5:3601–3614. https://doi.org/10.1039/C3NR00476G
47. Kalathil S, Khan MM, Ansari SA et al. (2013) Band gap narrowing of titanium dioxide (TiO_2) nanocrystals by electrochemically active biofilms and their visible light activity. Nanoscale 5:6323–6326. https://doi.org/10.1039/c3nr01280h

48. Zhang Y, Xu X (2020) Machine learning band gaps of doped-TiO_2 photocatalysts from structural and morphological parameters. ACS Omega 5:15344–15352. https://doi.org/10.1021/acsomega.0c01438
49. Singh M, Goyal M, Devlal K (2018) Size and shape effects on the band gap of semiconductor compound nanomaterials. J Taibah Univ Sci 12:470–475. https://doi.org/10.1080/16583655.2018.1473946
50. Yan H, Zhao T, Li X, Hun C (2015) Synthesis of Cu-doped nano-TiO_2 by detonation method. Ceram Int 41:14204–14211. https://doi.org/10.1016/j.ceramint.2015.07.046
51. Sreekantan S, Zaki SM, Lai CW, Tzu TW (2014) Copper-incorporated titania nanotubes for effective lead ion removal. Mater Sci Semicond Process 26:620–631. https://doi.org/10.1016/j.mssp.2014.05.034
52. Chan GH, Zhao J, Hicks EM et al. (2007) Plasmonic properties of copper nanoparticles fabricated by nanosphere lithography. Nano Lett 7:1947–1952. https://doi.org/10.1021/nl070648a
53. Bessekhouad Y, Robert D, Weber JV (2004) Bi_2S_3/TiO_2 and CdS/TiO_2 heterojunctions as an available configuration for photocatalytic degradation of organic pollutant. J Photochem Photobio A Chem 163:569–580. https://doi.org/10.1016/j.jphotochem.2004.02.006
54. Serpone N, Maruthamuthu P, Pichat P et al. (1995) Exploiting the interparticle electron transfer process in the photocatalysed oxidation of phenol, 2-chlorophenol and pentachlorophenol: chemical evidence for electron and hole transfer between coupled semiconductors. J Photochem Photobio A Chem 85:247–255. https://doi.org/10.1016/1010-6030(94)03906-B
55. Marschall R (2014) Semiconductor composites: strategies for enhancing charge carrier separation to improve photocatalytic activity. Adv Funct Mater 24:2421–2440. https://doi.org/10.1002/adfm.201303214
56. Liu M, Qiu X, Miyauchi M, Hashimoto K (2011) Cu(II) oxide amorphous nanoclusters grafted Ti^{3+} self-doped TiO_2: An efficient visible light photocatalyst. Chem Mater 23:5282–5286. https://doi.org/10.1021/cm203025b
57. Xiong L, Yang F, Yan L et al. (2011) Bifunctional photocatalysis of TiO_2/Cu_2O composite under visible light: Ti^{3+} in organic pollutant degradation and water splitting. J Phys Chem Solids 72:1104–1109. https://doi.org/10.1016/j.jpcs.2011.06.016
58. Chiang K, Amal R, Tran T (2002) Photocatalytic degradation of cyanide using titanium dioxide modified with copper oxide. Adv Environ Res 6:471–485. https://doi.org/10.1016/S1093-0191(01)00074-0